Research Article | Vol. 27, No. 10 | 13 May 2019 | OPTICS EXPRESS 13991
Optics EXPRESS

Relay optical function and pre-construction results of a Giant Steerable Science Mirror for a thirty meter telescope

YANG FEI,[1,*] ZHANG XUEJUN,[1] ZHAO HONGCHAO,[1] AN QICHANG,[1] GUO PENG,[1] JIANG HAIBO,[1] CAO HAIFENG,[1,2] GUO PENGFEI,[1] LUO XIAO,[1] QI ERHUI,[1] HU HAIFEI,[1] HU HAIXIANG,[1] ZHANG JING,[3] TOMAS CHYLEK,[4] GLEN COLE,[4] MYUNG CHO,[5] BYRON SMITH,[6] AND MARVIN CAMPBELL[7]

[1]*Changchun Institute of Optics, Fine Mechanics and Physics, Chinese Academy of Sciences, Changchun 130033, China*
[2]*University of Chinese Academy of Sciences, Beijing 100039, China*
[3]*Changchun University of Science and Technology, Changchun 130022, China*
[4]*TMT International Observatory, Pasadena, CA 91101, USA*
[5]*National Optical Astronomy Observatory, Tucson, AZ 85710, USA*
[6]*X Double Dot, LLC, Flagstaff, AZ 86001, USA*
[7]*Titan Advanced Solutions, Garland, TX 75044, USA*
**yangf@ciomp.ac.cn*

Abstract: The Giant Steerable Science Mirror (GSSM) is the tertiary mirror system of the Thirty Meter Telescope (TMT) that relays optical beams from the secondary mirror to active instruments on Nasmyth platforms. One of the key technologies involved in GSSM functions is the error budget allocation from the system engineering of TMT. A novel approach of error analysis and allocation with strong adaptability, which is based on normalized Point Source Sensitivity (PSSn), is proposed. The relay optical function including the quality of the wavefront, the rationality of the mechanism, and the stability of the light were achieved based on the proposed method. The experiments validate the proposed method.

1. Introduction

The Thirty Meter Telescope (TMT) is a large telescope that has unique capabilities enabling it to address questions that cannot be answered by current telescopes. With a 30 m primary mirror, TMT has nine times the light-gathering ability and three times the linear resolution of a Keck telescope, making it the second largest telescope in the world after E-ELT. The combination of light-gathering power and resolution enhances the point-source sensitivity by more than 80 times that of a 10-m telescope (sensitivity scales as D^4). TMT is designed to transmit light from 310 nm to 28,000 nm, allowing its instruments to characterize objects using a broad range of multiple wavelength bands. Other large telescopes are not designed to have such a broad wavelength coverage [1–6].

TMT is an international cooperation project initiated by the United States, Canada, Japan, India, and China. Changchun Institute of Optics, Fine Mechanics and Physics, Chinese Academy of Sciences (CIOMP) is mainly responsible for the development of the TMT tertiary mirror system, which is also called Giant Steerable Science Mirror (GSSM) as shown in Fig. 1. As the largest elliptical plane mirror (3594 mm × 2536 mm × 100 mm), the GSSM has not only the general light transmit function but also the precision pointing function [7–10]. Therefore, GSSM has a unique optical relay function and it is faced with many technical challenges. In order to reduce the risk of technology and construction, a scaled prototype is developed to enhance the feasibility of optical relay function.

This paper is organized as follows: Section 2 presents the error analysis and allocation by normalized point source sensitivity (PSSn). Section 3 presents the GSSM cell assembly and

#360448 https://doi.org/10.1364/OE.27.013991
Journal © 2019 Received 18 Feb 2019; revised 9 Apr 2019; accepted 18 Apr 2019; published 30 Apr 2019

Optics EXPRESS

its measurement. PSSn was increased from 0.6791 to 0.7532 after warping harness correction. Section 4 presents the GSSM positioner assembly and its measurement. The systematic measurement error was 3" for the tilt axis and 2.3" for the rotation axis. At 0° zenith angle, the repeatability error was 1.9 " and at 10° zenith angle, the error was 2.6". Section 5 presents the GSSMP jitter and its measurement. The tracking error, the main index for evaluation of system jitter, was 13.3 mas (rotation) and 18.4 mas (tilt) in the form of RMS.

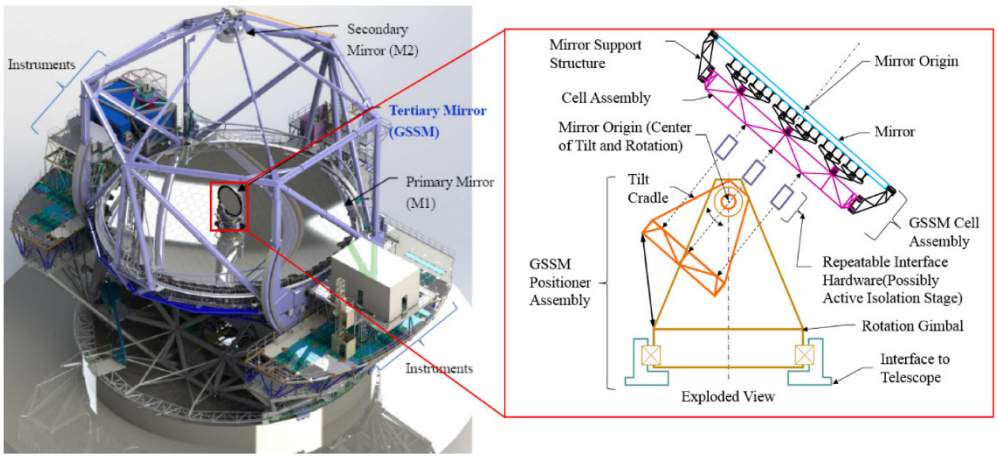

Fig. 1. Configuration of TMT and GSSM. Since the system has many scientific instruments located on both sides of the platform, the tertiary mirror along with the telescope pointing movement will relay light beams to various science instruments.

2. Basic principle

2.1. Error analysis and allocation in GSSM

Building a large telescope with an aperture of 30 m and working near the diffraction limit is a significant challenge for both design and construction.

PSSn utilizes the integral average in all areas of optical transfer function (OTF) and considers the effects of the background. Additionally, PSSn has good composing characteristics, which can easily cover a variety of error factors [11,12].

In the analysis of the synthesis characteristics of PSSn, according to the principle of Taylor expansion, PSSn decreases due to the increase of the error, thus, the error approximates the second order polynomial, assuming an error function $\varepsilon_i(\vec{r}) \approx a_i \vec{r}^2$ where a_i is a constant and $\vec{r}$ is the two-dimensional coordinates for the optical path difference (OPD) (typically in meter units).

The composition error is shown in Eq. (1):

$$\delta \equiv \left\langle \varepsilon_1(\vec{r})\varepsilon_2(\vec{r}) \right\rangle - \left\langle \varepsilon_1(\vec{r}) \right\rangle \left\langle \varepsilon_2(\vec{r}) \right\rangle \approx a_1 a_2 \left(\left\langle r^4 \right\rangle - \left\langle r^2 \right\rangle^2 \right) \tag{1}$$

where $\langle \cdot \rangle$ defines a new operator, *average of atmosphere* [13],

Since $PSSn_i = 1 - \left\langle \varepsilon_i(r) \right\rangle \approx 1 - a_i \left\langle r^2 \right\rangle$, Eq. (1) can be expressed as Eq. (2):

$$\delta \approx \frac{\left(\left\langle r^4 \right\rangle - \left\langle r^2 \right\rangle^2 \right)}{\left\langle r^2 \right\rangle^2} (1 - PSSn_1)(1 - PSSn_2) = 1.2119 (1 - PSSn_1)(1 - PSSn_2) \tag{2}$$

Since PSSn is relatively small, the error decreases as the number of synthetic items increases, which is also an advantage of PSSn as an evaluation index. By probabilistically

studying the Slope RMS, the probability distribution of the evaluation scale corresponding to different components of the telescope can be obtained. Let i, j be the state i and state j, and l_{ij} refers to the process from state i to state j. Assuming that its value is discrete, its distribution rate is $P\left(l_{ij}=l_k\right)$. Using the eigenfunction $M_{l_{ij}}(t)$ of the probability density function, i.e., the expectation of the moment generating function, the statistical moment of each random variable can be obtained as shown in Eq. (3) [14],

$$M_{l_{ij}}(t)=E\left(e^{tl_{ij}}\right)=\sum_{l_k=1}^{\infty}e^{tl_k}P\left(l_{ij}=l_k\right) \tag{3}$$

where t is an independent variable of the characteristic function and is set to a real number.

The transfer function between the elements is set as $T_{ij}=P_{ij}M_{l_{ij}}(t)$ using the properties of the characteristic function $M_{l_{ij}}(t)$, where P_{ij} is the transition probability.

After modeling, the overall transfer function $T_{Tot}(x)$ of the system can be obtained. Using the sequence expansion method of the cosine function, the probability density function can approximate the numerical solution as shown in Eq. (4).

$$f_{Tot}(k)=\frac{1}{b-a}\sum_{m=0}^{N-1}\left[T_{Tot}^{*}\exp\left(\frac{\sqrt{-1}m\pi}{b-a}\right)+T_{Tot}\exp\left(\frac{\sqrt{-1}m\pi}{b-a}\right)\right]\cos\left(m\pi\frac{l_k-a}{b-a}\right) \tag{4}$$

The interval $[a,b]=[\min(x),\max(x)]$ corresponds to the probability density function $f_{Tot}(x)$. The cumulative probability is presented in Eq. (5).

$$p(l_{ij}=l_k)=\sum_{u=0}^{k}f_{Tot}(u) \tag{5}$$

Since the method generates the transfer function of the system, $\left\langle l_{ij}\right\rangle$ and $VAR(l_{ij})$ can also be obtained. Initial scale of the system is set to the atmospheric coherence length. Its original probability distribution affects the statistical characteristics of the subsequent links.

According to previous research, the general process of error analysis and allocation of GSSM can be obtained using the good synthetic and decomposing properties of PSSn to determine the static and dynamic wavefront error and pointing error of the system. Using the slope root mean square (Slope RMS), which is a computationally-friendly metric, establishes the relationship between the actual working conditions of the telescope and PSSn. Corresponding to the actual components, the connection between the abstract subsystems can be statistically established and the likelihood function can be used to assist system engineers to make decisions on error analysis and the allocation of large-aperture telescopes.

In the proposed process, we calculate the statistical moments of all orders (expectation, variance). The probability model is key to completing these steps. Compared with the traditionally used Gaussian process, the statistical characteristics are no longer independent or identically distributed due to the influence of the system feature boundary conditions. Using the stochastic engineering eigenvalue theory [15], complex random processes can be expressed as the sum of a series of simpler random processes, which simplifies the analysis process. Using the linear combination of stochastic processes to obtain a probability model that conforms to the special boundary conditions, eigenvalues and the characteristic function can be used to complete the model construction.

The following analysis shows the applications of the “Brownian bridge” process and the allocation of large-aperture telescope errors. Error analysis and distribution are statistically significant processes. An error evaluation index must evaluate the performance and consider

Optics EXPRESS

the statistical characteristics of the error. From a statistical point of view, PSSn can be a better error distribution criterion. From a stochastic point of view, if a process reaches a certain state with a probability of 1 after a few steps, it is called the Brownian bridge process and denoted as $B(t)$.

Similar to the Wiener process, the related function of the Brownian bridge process satisfies Eq. (6) [16],

$$E\left[B(t)B(t+v)\right]=\frac{t}{T}-\frac{t(t+v)}{T^2} \tag{6}$$

where T is the time to reach a certain state with probability 1. By solving the eigenvalues of the stochastic process, we obtain Eq. (7),

$$\Psi(t)=\lambda\int_0^T E\left[B(t)B(t+v)\right]\Psi(v)\,dv \tag{7}$$

where $\Psi(t)$ is the characteristic function of the Brownian bridge process, which satisfies Eq. (8) and λ is the eigenvalue of the Brownian bridge process.

$$\int_0^T \Psi^2(t)\,dt=1 \tag{8}$$

In fact, the Brownian bridge process can be obtained through the Wiener process $W(t)$

$$B(t)=\sigma\left[W(t)-tW(1)\right] \tag{9}$$

where $0\le t\le 1$. The characteristics of $W(t)$ are shown in Eq. (10).

$$E\left[e^{-tW^2(t)}\right]=\sqrt{\sin c\left(\sqrt{2t}\right)} \tag{10}$$

We combine Eq. (9) with Eq. (10) to obtain Eq. (11):

$$E\left[e^{-B^2(t)}\right]=E\left[e^{\sigma^2\left[-W^2(t)+2tW(1)W(t)-t^2W^2(1)\right]}\right]=2e^{-\sigma^2t^2}\sqrt{\sin c(2t)} \tag{11}$$

We take the logarithm on both sides of Eq. (11) to obtain Eq. (12).

$$E\left(B^2(t)\right)=\frac{1}{2}\sigma^2t^2-\ln(2)\ln\left(\sin c\left(\sqrt{2t}\right)\right) \tag{12}$$

The error models that are completely independent of each other and that obey Gaussian distribution are close to those of the Wiener process. Owing to different error models, the variance of the system also changes. The Brownian bridge process considers the error chain closure and can effectively reduce the overestimation in error analysis and assignment.

Assuming that $\lambda=k^2$, $\Psi(t)=\sin kt$, we define Brownian bridge in continuous time as shown in Eq. (13).

$$B(t)=\sum_{n=1}^{\infty}\frac{1}{\sqrt{\lambda_n}}\Psi_n(t)X_n(t)=\sum_{n=1}^{\infty}\frac{\sqrt{2}}{\pi n}\sin(\pi nt)X_n(t) \tag{13}$$

The Brownian bridge is expressed as a discrete process, i.e., the time to reach a certain state with probability 1. Time is replaced by the number of transition steps as shown in Eq. (14).

Optics EXPRESS

$$B_i = \sum_{n=1}^{N-1} \frac{\sqrt{2}\sin(\pi in/N)}{\sin(\pi n/2N)} X_n \tag{14}$$

Taking the segment tilt of the sparse-aperture telescope as the research objective, we can evaluate the application of Brownian bridge in the error analysis and allocation of large-aperture telescopes. Since there is a position sensor between the segments, the absolute positional accuracy of each segment cannot be guaranteed. However, considering the loop formed by any segments, the final position error must be the position measurement residual of the sensor. In a Keck telescope, the tilt of the segment can be considered the local slope change of the entire mirror in the calculation of the system scale. By using the relationship between PSSn and RMS, the segment tilt PSSn can be derived by $1-PSSn \approx \alpha\sigma^2$ where σ is the RMS WFE and α is a proportional constant independent to σ. However, α is a function of aberration frequency (correlation length of OPD) and atmosphere r_0.

Considering that the traditional RMS, PV and other indicators cannot reflect the frequency domain characteristics of the mirror shape and Slope RMS can better reflect the intermediate frequency characteristics of large-scale optical components. Slope RMS is selected as the evaluation index of the mirror shape. Moreover, Slope RMS has a statistically significant conversion relationship with PSSn, which also provides great convenience for converting the surface error into the more comprehensive unified evaluation standard. The calculation process of Slope RMS is simpler than PSSn and can reduce the system engineering requirements for numerical calculation of the resources. Meanwhile, the slope field is a non-conservative field and the integration result is related to the integration method and the path. Therefore, it is very difficult to use slope information to recover the wave. We can combine PSSn with the Slope RMS. By using the slope of the wavefront, an error model with higher computational efficiency can be established to further improve the cost-effectiveness of integrated detection.

The relationship between PSSn and Slope RMS is given by [17]

$$1-PSSn \approx \mu r_0^2 \left(\frac{2\pi}{\lambda}\right)^2 \frac{SlopeRMS^2}{4\pi^2} = \gamma \frac{SlopeRMS^2}{\lambda^2} \tag{15}$$

where $\gamma = \mu r_0^2$. μ is a dimensionless constant, r_0 is a Fried parameter, *SlopeRMS* is in units of *rad/m*, and λ is the wave-length in for computing the PSSn.

Using the formula shown as above, we can obtain an expression for PSSn under Brownian bridge as shown in Eq. (16), where N is the number of transfer steps divided by the number of error sources.

$$E\left(B_i^2\right) \approx \sum_{n=0}^{N-1} \frac{1}{2} SlopeRMS_n^N \left(\frac{\pi n}{N}\right)^2 - \ln(2) \sum_{n=0}^{N-1} \ln\left(\sin c\left(\sqrt{2\left(\frac{\pi n}{N}\right)}\right)\right) \tag{16}$$

Assuming that the error chain is completely closed, without considering the residual error, the modified probabilistic model is presented as follow

$$1-PSSn_c \approx \mu r_0^2 \left(\frac{2\pi}{\lambda}\right)^2 \frac{\sum_{n=0}^{N-1} \frac{1}{2} SlopeRMS_n^N \left(\frac{\pi n}{N}\right)^2 - \ln(2) \sum_{n=0}^{N-1} \ln\left(\sin c\left(\sqrt{2\left(\frac{\pi n}{N}\right)}\right)\right)}{2\pi^2} \tag{17}$$

By establishing the mathematical model of the connection between PSSn and Slope RMS, PSSn's good synthesis and decomposition characteristics and Slope RMS's computationally-friendly properties can be effectively utilized. This model can effectively improve the efficiency of error analysis and allocation in telescope design and construction.

2.2. GSSM cell assembly (CA) measurement

The GSSM CA testing and evaluation process is shown in Fig. 2. First, interferometer data for further processing are collected. Then, targets are set for coordinate system alignment and error estimates. After putting the full mirror data together, according to the projection of the system entrance pupil on GSSM, the footprint is intercepted. Prior to the interception of the footprint, the elliptical mirror data should be circularized and the focus and astigmatism should be calculated to characterize low-order surface aberration [18–22]. After cutting the footprints and removing the own piston and tilt component, Slope RMS and PSSn are evaluated using Eq. (18).

$$1-PSSn \approx \frac{\gamma\sigma_{slope}^2}{\lambda^2} \tag{18}$$

where γ is 0.11 m^2/rad^2, λ is the wavelength (0.5 μm), and σ_{slope} is the Slope RMS.

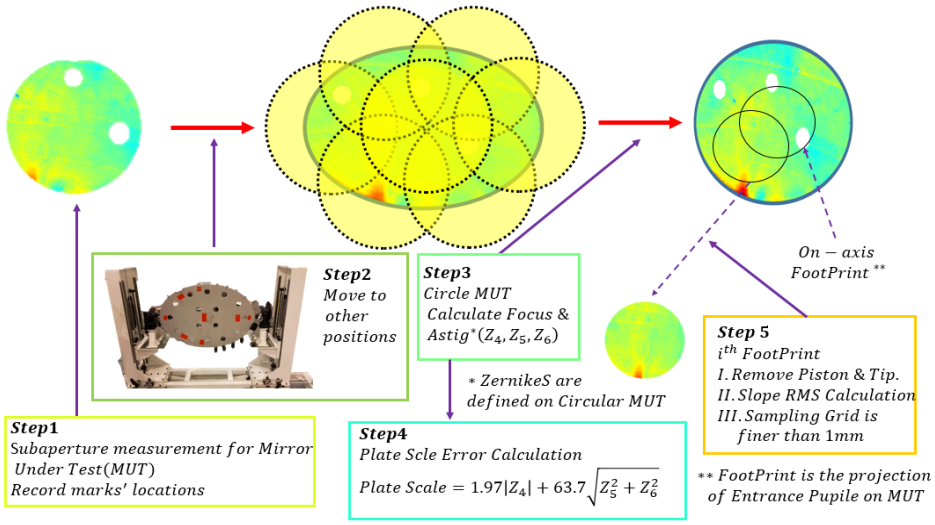

Fig. 2. GSSM CA testing and evaluation process. The evaluation index of 30-m telescope tertiary mirrors is based on slope and its evaluation is in sub-apertures.

Slope RMS is easy to calculate and associated with many traditional indices, as shown in Fig. 3. Spherical aberration produced by a single-aperture telescope under the action of a thermal load can be taken as an example. The overall wavefront $\Phi_{SPh}(x,y)$ is shown as

$$\Phi_{SPh}(x,y) = \alpha_{11}\sqrt{5}\left(6\rho^4 - 6\rho^2 + 1\right) \tag{19}$$

where ρ is the radius of wavefront and α_{11} is the first-order spherical aberration coefficient of the overall wavefront defined by Noll. The slope of the spherical aberration of the overall wavefront in x/y direction are expressed by

$$\Phi_{Sph\_x}^{S}(x,y) = \alpha_{11}\sqrt{5}\left(12\rho^3\cos\theta - 12\rho\cos\theta\right) \tag{20}$$

$$\Phi_{Sph\_y}^{S}(x,y) = \alpha_{11}\sqrt{5}\left(12\rho^3\sin\theta - 12\rho\sin\theta\right) \tag{21}$$

The average slope of the overall wavefront spherical aberration is shown in Eq. (22).

$$\left\langle \Phi_{Sph\_x}^{S}(x,y)\right\rangle = \left\langle \Phi_{Sph\_y}^{S}(x,y)\right\rangle = 0 \tag{22}$$

Optics EXPRESS

The slope of the overall wavefront spherical aberration is shown in Eq. (23), where R denotes the wavefront radius.

$$\left\langle \left(\Phi^{S}_{Sph\_x}\right)^2 \right\rangle = \left\langle \left(\Phi^{S}_{Sph\_y}\right)^2 \right\rangle = 2\alpha_{11}^2 R^2 \left(45R^4 - 120R^2 + 90\right) \tag{23}$$

The Slope RMS represented by polar coordinates can be obtained by Eq. (24).

$$\sigma_{Slo}\sqrt{\left\langle \left(\Phi^{S}_{Sph\_x}\right)^2 \right\rangle + \left\langle \left(\Phi^{S}_{Sph\_y}\right)^2 \right\rangle} = \sqrt{2}\alpha_{11} R\sqrt{45R^4 - 120R^2 + 90} \tag{24}$$

Considering the normalized properties of the Zernike polynomial, the ratio of the Slope RMS to the RMS is given by Eq. (25).

$$\frac{\sigma_{Slo}}{\sigma_{RMS}} = \sqrt{2}R\sqrt{45R^4 - 120R^2 + 90} \tag{25}$$

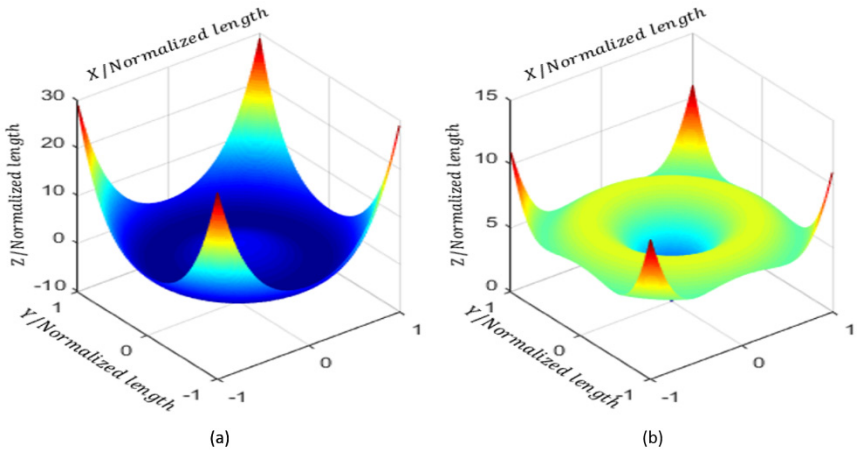

Fig. 3. Relationship between the optical error of the system and the Slope RMS of the system: (a) The initial spherical aberration of the system (b) Slope RMS.

In order to balance accuracy and cost, the subaperture stitching technology is introduced for large planar mirror testing. Similar to the region-based wavefront reconstruction method, which has a certain overlap between various subapertures, the relative piston and relative tilt between each subaperture should be considered [23–25]. For the general measurement system, the measurement data of the system is overdetermined. The most common model is the Gauss Markov model [26]:

$$\begin{cases} L_{PSSn} = AX + \Delta \\ E(\Delta) = 0; \mathrm{cov}(\Delta) = \sigma_0^2 P^{-1} \end{cases} \tag{26}$$

where L_{PSSn} is the measurement matrix, A is matrix of coefficients, X is the matrix of principal parameters, Δ is the observation error matrix, σ_0^2 is the matrix of parent unit weight, and P is the weight matrix.

The true difference vector can be estimated using $e = \hat{x} - x$.

Considering the least squares solution $\hat{x}_{LS} = \left(A^T PA\right)^{-1} A^T PL_{PSSn}$, due to its unbiased nature $bias(\hat{x}) = 0$, the estimated mean square error is:

$$E\left(e^T e\right) = trace\left[\mathrm{var}\left(\hat{x}_{LS}\right)\right] \tag{27}$$

Optics EXPRESS

Setting up additional systems with all the parameters $X=(x_1,x_2)$:

$$\begin{cases} L_{PSSn}=(A_1,A_2)(x_1,x_2)^T+\Delta \\ E(\Delta)=0;\mathrm{cov}(\Delta)=\sigma_0^2P^{-1} \end{cases}$$

where $N_{11}=A_1^TPA_1$, $N_{12}=A_1^TPA_2$, $N_{22}=A_2^TPA_2$. Equation (27) is rewritten as Eq. (28):

$$E_{basic}(e^Te)=\sigma_0^2 trace\left[N_{11}^{-1}+\left(N_{11}^{-1}N_{12}\right)^TQ_{X_2X_2}N_{11}^{-1}N_{12}\right] \tag{28}$$

where $Q_{vv}=P^{-1}-A_1N_{11}^{-1}A_1^T$, $Q_{X_2X_2}=\left(A_2^TPQ_{vv}P^TA_2\right)^{-1}$.

The estimation of the reduced parameter model is obtained as $\overline{x}_1=\left(A_1^TPA_1\right)^{-1}A_1^TPL_{PSSn}$. The estimated mean square error is given by

$$E_{sub}(e^Te)=\sigma_0^2 trace\left[N_{11}^{-1}+\left(N_{21}N_{11}^{-1}\right)^TM^{-1}\left(N_{21}N_{11}^{-1}\right)\right]+trace\left[\left(N_{11}^{-1}N_{12}x_2^T\right)^T\left(N_{11}^{-1}N_{12}x_2^T\right)\right] \tag{29}$$

where $\mathrm{M}=N_{22}-N_{12}^TN_{11}^{-1}N_{12}$.

Adjusting the model by using the orthogonal base, Eq. (29) can be simplified.

$$\Delta E=E_{basic}(e^Te)-E_{sub}(e^Te) \tag{30}$$

When $|P|=1$, then $(P_{11}+P_{22}+\cdots+P_{nn})/n\geq\prod P_{ii}=1$ and for the diagonal matrix, $\sigma_0^2 trace(P)\geq n\sigma_0^2$.

By selecting the proper coordinate origin as $E(x_2)=0$ to make it $x_2x_2^T=n_2\sigma_{x2}^2$ and $\sigma_0^2\approx\left[(n-n_2)\sigma_{x1}^2+n_2\sigma_{x2}^2\right]/n$ then,

$$\Delta E=E_{basic}(e^Te)-E_{sub}(e^Te)\geq n\sigma_0^2-n_2\sigma_{x2}^2\approx(n-n_2)\sigma_{x1}^2 \tag{31}$$

In actual testing, noise reduction is an important step. Generally, it can adapt the method of averaging on a small scale to constrain noise or it can use a filtering process such as the singular value method. Using a singular value, it understands the system's main component and constrains the noise [27–31].

The basic method to consider exposure time is to use the exposure function to add window processing in the calculation of the system frequency domain metric. Exposure time can be considered when using the wavefront power spectrum to calculate the RMS.

$$\sigma^2(\tau)=\int_0^{f_n}PSD(f)\left[1-\sin c^2(\tau f)\right]df \tag{32}$$

where f is the space frequency, σ is the error RMS, τ is the exposure time, and $PSD(f)$ is the wave front error power spectrum. The integral region is $[0,f_n]$. According to the method of processing exposure time introduced in Eq. (32), the final expression of PSSn can be obtained by

$$PSSn_\tau=\prod\lim_{i\to\infty}\left(1-\int_{f_i}^{f_{i+1}}\beta(f)\left[1-\sin c^2(\tau f)\right]PSD(f)2\pi f df\right) \tag{33}$$

Optics EXPRESS

where $\beta(f)=\begin{cases}\mu r_0 f^2 & (f<\frac{1}{r_0}circle/rad)\\ 2 & (f\geq\frac{1}{r_0}circle/rad)\end{cases}$.

According to the traditional method, the large-aperture planar mirror will improve its own requirements to realize the expected function in increasingly complicated working conditions. Warping harness, which is a large-flat mirror assembly technology, can correct the deformation caused by gravity and heat load under a single working condition. The warping method is based on the linear theory, which is used to add the results of the individual actions of various torque actuators directly. The Giant Steerable Science Mirror Prototype (GSSMP) mirror figure correction process is shown in Fig. 4.

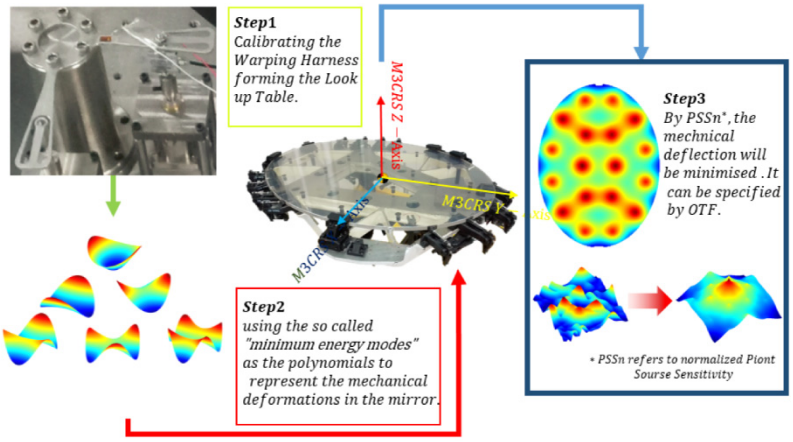

Fig. 4. GSSMP mirror figure correction. For the later moment correction, it is important to shift the actual pivot position in space. For a single gravity condition, it can be balanced by drilling.

System performance index is set to $PSSn$. The change in the performance index is and the correct torque is $\Delta\mathbf{u}$. The system performance index $PSSn$ can be derived through Taylor expansion by

$$\Delta PSSn=\frac{\partial PSSn}{\partial\mathbf{u}}\Delta\mathbf{u}+o\left(\Delta\mathbf{u}^2\right) \tag{34}$$

To obtain the gradient of the performance, multiply $\Delta\mathbf{u}^T$ on both sides of the Eq. (34).

$$\left\langle\Delta PSSn\Delta\mathbf{u}^T\right\rangle=\left\langle\frac{\partial PSSn}{\partial\mathbf{u}}\Delta\mathbf{u}\Delta\mathbf{u}^T\right\rangle+\left\langle o\left(\Delta\mathbf{u}^2\Delta\mathbf{u}^T\right)\right\rangle \tag{35}$$

The elements in $\Delta\mathbf{u}$ are independent and evenly distributed and RMS of $\Delta\mathbf{u}$ is σ. Equation (36) outputs the unbiased estimation of the gradient of the evaluation index by the statistical rule.

$$\left\langle\frac{\partial PSSn}{\partial\mathbf{u}}\right\rangle=\left\langle\Delta PSSn\Delta\mathbf{u}^T\right\rangle/\sigma^2 \tag{36}$$

$$\mathbf{u}^{n+1}=\mathbf{u}^n+\Delta PSSn\Delta\mathbf{u}^T/\sigma^2 \tag{37}$$

Using the mathematical model between Slope RMS and PSSn, the mathematical relationship between the warning harness and the evaluation index of the mirror figure is

derived, which theoretically illustrates the important role of the warning harness correction in improving the figure quality of GSSM.

2.3. GSSM position assembly (PA) measurement

Large telescopes are subject to various motions such as the deformation of the tracking mount of the telescope itself or the motion caused by the temperature gradient. The purpose of calibration is to meet the TMT's requirements and it is a procedure for removing unnecessary systematic effects from measurements. Calibration allows the GSSM to achieve a higher level of accuracy [32–36].

For GSSM, the rotation angle is

$$\theta = \arctan\left(\frac{\cos(\zeta)\cos(IEA)\sin(IBA)+\sin(\zeta)\sin(IEA)}{\cos(IEA)\cos(IBA)}\right)$$

and the tilt angle is $\Phi = 0.5\arccos\left(-\sin(\zeta)\cos(IEA)\sin(IBA)+\cos(\zeta)\sin(IEA)\right)$, where ζ is zenith angle of telescope, which is limited from 1° to 65° for observation, IEA and IBA are Instrument Elevation Angle and Instrument Bearing Angle respectively.

$$\frac{d\theta}{dt} = E^{'}\frac{\cos(E)\sin(IBA)/\cos(IBA)-\sin(E)\sin(IEA)/\left[\cos(IEA)\cos(IBA)\right]}{\left(\left[\sin(E)\cos(IEA)\sin(IBA)+\cos(E)\sin(IEA)\right]\cos(IBA)/\cos(IEA)\right)^{2}+1} \quad (38)$$

and

$$\frac{d\Phi}{dt} = E^{'}\frac{\sin(E)\cos(IEA)\sin(IBA)+\cos(E)\sin(IEA)}{-2\sin\left(\operatorname{acos}\left(-\cos(E)\cos(IEA)\sin(IBA)+\sin(E)\sin(IEA)\right)\right)} \quad (39)$$

where E is the telescope elevation angle, $E^{'}$ is telescope elevation angular velocity, and $E^{'}_{\max} = 15.522\,\text{arcsec/sec}$.

In order to meet the stringent position accuracy requirements of GSSM, the calibration accuracy level of GSSM is improved by establishing a mathematical model between GSSM and IEA and IBA.

2.4. GSSM jitter measurement

GSSM collects light and transmits it to the instruments located on each side of the platform. Because of its long transmission distance, the influence of jitter is larger in GSSM than in SOAR and VISTA (both 4-m telescopes) with more complex requirements. Jitter feature plays an important role in the completion of GSSM system functions. In order to evaluate the light relay function, GSSM needs to integrate the acceleration signal into the angular displacement signal [37–41].

3. Experiment

3.1. GSSM position assembly (PA) measurement

In order to better realize the relay optical function of GSSM, TMT has set many requirements for GSSM's motion. To verify these motion requirements, all the precision specifications of GSSM are based on the rigid body displacement of the plane mirror and then the relay function of the light is converted. By collecting basic geometric elements, a simpler and more convenient model can be built. The rotation of the mirror axis is used to define the coordinates of the x-y plane and z axis.

Calibration is performed to set or correct a measuring device or the base level by adjusting it to match a trusted and constant measurement. The suppression part is the systematic error,

Optics EXPRESS

thus, the repeatability error of a single point is important for the estimation of system error. The pointing repeatability at different zenith angles is shown in Fig. 5. When zenith angle is 0, the repeatability is 1.9" and when zenith angle is 10°, the repeatability is 2.6".

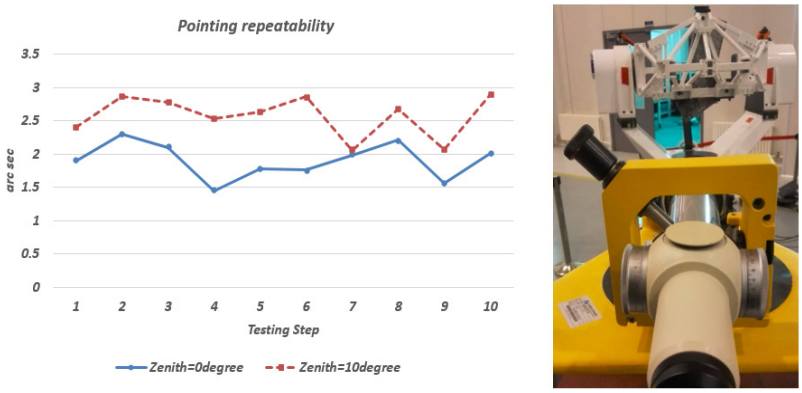

Fig. 5. GSSMP pointing repeatability testing. Repeatability is the foundation of calibration. The system of two axes disjoints and two axes are not perpendicular. Calibration can be used for inhibition

The GSSM encoder readings are calibrated using lookup tables that adjust encoder settings so that the correct pointing angles can be reached under varying gravity directions and temperatures (Fig. 5). In GSSMP testing, the systematic measurement error is 11.9" for the tilt axis and 9.2" for the rotation axis as shown in Fig. 6 (down left).

According to the design requirements of TMT, the M3 system (M3S) can rotate the M3 mirror about the Elevation Coordinate Reference System (ECRS) Z-axis to any angle within the range of a repeatable residual M3 rotation error (after telescope calibration) less than 3.5" RMS.

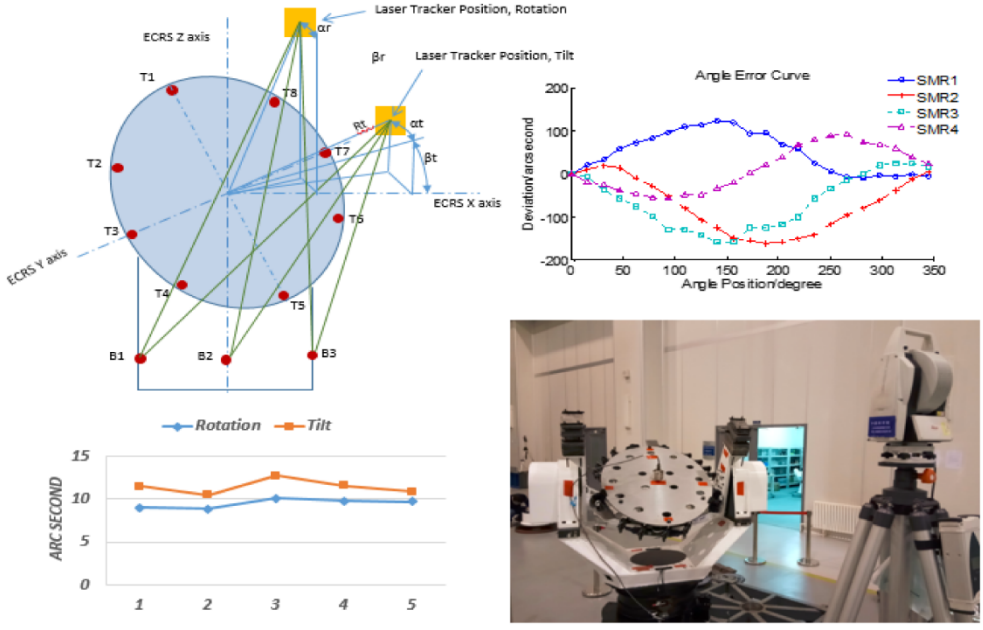

Fig. 6. GSSMP calibration sketch. Using laser tracker, calibration precision can reach 10 arc seconds. With the enlargement of the radius of bearings, its precision will improve

Optics EXPRESS

3.2. GSSM jitter measurement

The jitter testing process is shown in Fig. 5, and the testing result is shown in Fig. 7. Systematic jitter is 13.3 mas (rotation) and 18.4 mas (tilt) in the form of RMS, after high-pass filters simulating tracking and adaptive optics (AO) corrections.

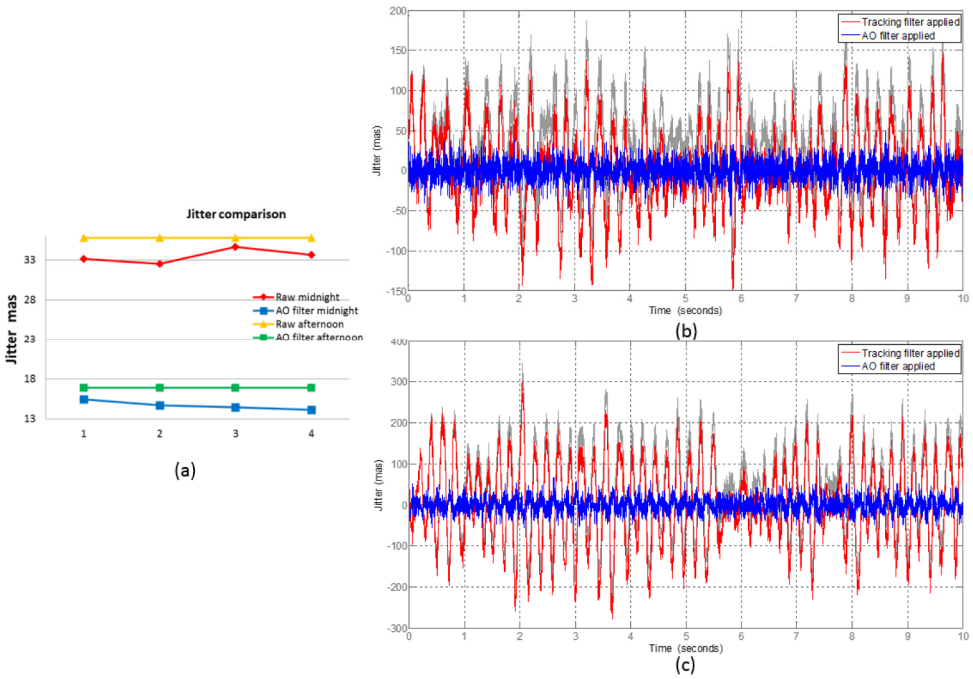

Fig. 7. GSSMP jitter testing (a) the testing result: X-axis is sequence number of test and y-axis is Jitter (mas) (b) the testing result of rotation axis (c) the testing result of tilt axis

The PSSn of GSSMP under different jitter levels can be obtained by the optical transfer function (Fig. 8). The attenuation of PSSn with vibration is linear. GSSMP can be predicted as PSSn at different jitter levels. Generally, for the ideal flat mirror under the influence of vibration, there is a small motion, resulting in very short time averages as the actual optical transfer function [42–47]. According to previous research, the optical transfer function of an ideal system under vibration influence is 0 Bessel function of first kind.

Optics EXPRESS

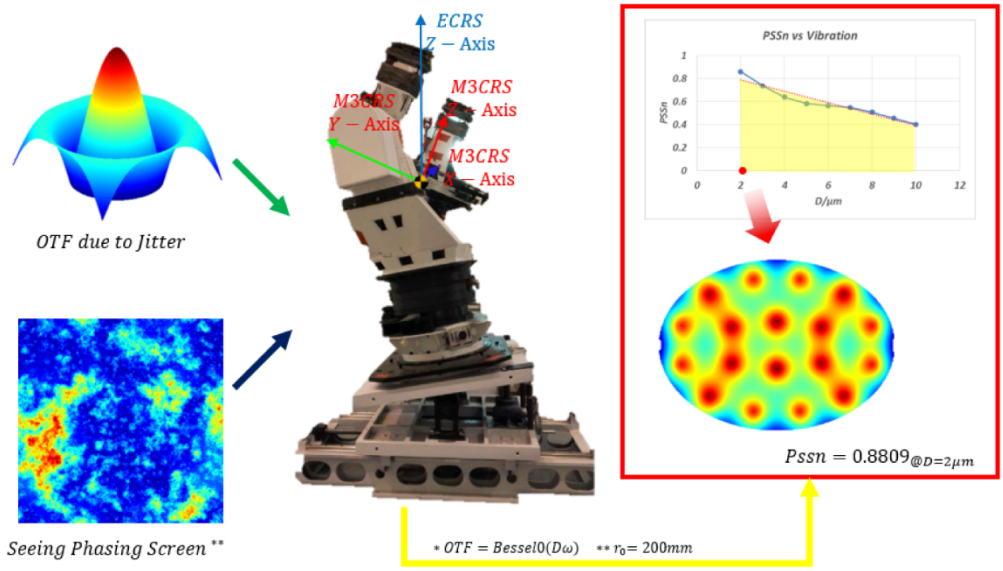

Fig. 8. GSSMP jitter influence on PSSn. For the telescope, when designing indicators related to vibration, we need to consider the backend adaptive optics correction ability

3.3. Warping harness correction

In order to verify the effect of Warping Harness to correct the mirror shape of M3 in TMT, calibration experiments were performed under six different work conditions (W1~W6) as shown in Table 1 where the gravity load is minimum and maximum in three directions (X, Y, Z), respectively.

Table 1. Warping harness in different work conditions

Work conditions	Before correction		After correction	
	RMS/nm	PSSn	RMS/nm	PSSn
W1	57.1	0.7156	20.7	0.7869
W2	35.3	0.8688	13.1	0.9085
W3	28	0.9338	10.5	0.9627
W4	29.3	0.9235	10.9	0.9512
W5	55.4	0.7391	19.9	0.8078
W6	59.5	0.6791	21.7	0.7532

By comparing the results before and after the correction, the following conclusions can be drawn:

1) In six different work conditions, the surface shape is increased by 71.79%(0.0713), 62.89%(0.0397), 62.5%(0.0289) 62.80%(0.0277), 64.08%(0.0687) and 63.53% (0.0741) in RMS (or PSSn), respectively, after correcting by Warping Harness. Warping harness can effectively improve the quality of mirror shape.

2) The smaller the angle between the direction of gravity and the z-axis in M3CRS, that is, the larger the projected area of the mirror in the direction of gravity, the better the correction effect of Warping Harness.

Optics EXPRESS

The above conclusions directly indicate that Warping Harness has a great effect on the quality of the mirror shape. Therefore, this method will be the preferred solution for semi-active optics in tertiary mirror system.

4. Discussion

The GSSM has the function of relay optics with desired accuracy and stability. In the stochastic process, each relay can be regarded as the transform of states. Combined with PSSn, it can realize the reasonable representation of various conditions of GSSM and facilitate the analysis and distribution of errors.

Due to the comprehensiveness of PSSn, the errors of different frequency bands can be appropriately covered. PSSn can effectively reduce the "overestimation" phenomenon in error analysis. Using the combination properties of PSSn, the error introduced by the mirror figure, atmospheric seeing, jitter, and other error sources can be synthesized to establish the error model of the system. The TMT M3 is a Giant Steerable Science Mirror system, which is the largest elliptical planar mirror system in the world today. It has the light folding function of the general flat and the precise pointing function, thus, it is necessary for the establishment of the system error model. Bottom-up error allocation is a comprehensive evaluation method for error sources based on an error evaluation metric, such as wavefront RMS, Slope RMS, power spectrum, or structure function.

The top-down evaluation method refers to the first comprehensive and profound understanding of each item in the error model. The top-down error evaluation method can reasonably distribute the error of each subsystem in the system according to the prior experience of the system engineers and it can effectively reduce the engineering cost and technical difficulty, and improve the engineering efficiency and quality.

The bottom-up evaluation method refers to the way in which the error distribution is performed from bottom to top according to the error distribution value of each end link in the error model. The bottom-up error distribution method can verify the error precision that the whole system can achieve in perfect operation according to the error precision actually achieved by each subsystem. The index precision can be approximated as the accuracy that can be achieved by the entire system when each subsystem is perfectly cooperative.

PSSn uses the integral average of all regions of the optical transfer function and fully considers the influence of the background on the optical energy transfer. Therefore, the top-down evaluation method can fully evaluate the imaging quality of the system. In contrast, PSSn has good linear synthesis characteristics, can be simple, and comprehensive errors under various influence factors can be obtained.

Note the unique advantages of top-down and bottom-up, and PSSn has good computational friendliness. Taking full advantage of the advantages of both, PSSn is used as an evaluation index to achieve a more scientific and effective error distribution for the error model. Firstly, the PSSn of each subsystem is roughly allocated according to the top-down evaluation method, and then the PSSn of the subsystem is verified by the experiment, and the rationality of the previously allocated PSSn is fully evaluated according to the bottom-up error evaluation method and the PSSn allocation is iterated. In this way, the effectiveness and rationality of error distribution can be greatly improved.

First, based on the prior engineering experience of the subsystem engineers, the system engineer performs preliminary error distribution on each subsystem. Note that the error distribution may not be perfect at this time. Then, the subsystem engineer performs experiments on the subsystem to obtain the results. The error accuracy that the system can actually achieve is then fed back to the system engineer. Based on the initial error distribution value and the actual error accuracy of the feedback by subsystem engineers, the system engineer fully considers the costs and technical risk in each subsystem, and appropriately adjusts and redistributes the error of each subsystem to achieve the adaptation and equalization of the error distribution of each subsystem. In this way, costs can be saved to the

Optics EXPRESS

maximum, technical risks can be avoided, and the efficiency and quality of error distribution can be greatly improved.

Considering the fact that the error is generally Gaussian with a mean of 0, we use PSSn as the evaluation index, establish the error distribution model based on the random statistical theory of Brownian bridge, and apply the method to the analysis and allocation of GSSM error. The feasibility of the model is proved.

The three error sources most relevant to the implementation of the optical relay function of GSSM are the rationality of the mechanism, the stability of the light and the quality of the wavefront. We conducted related experiments on the three error sources considered above. The experimental results show the effectiveness and feasibility of the proposed method. The testing results are summarized as shown in Table 2.

Table 2. The testing results of GSSMP

Item	Function	Measurement mode	Verification	Test results	Discussion
Relay optical function	Rationality of the Mechanism (Position Assembly)	Autocollimator + Laser Tracker	Analysis + Testing	The systematic measurement error 11.9" @tilt axis 9.2" @rotation axis	The experimental method is verified and will be used in the larger size of GSSM to meet the requirements of TMT.
	Stability of the Light (Jitter)	Accelerometer + Bassel Function + PSSn	Testing	RMS 13.3 mas @Rotate RMS 18.4 mas @Tilt	The experimental method is verified and will be used in the larger size of GSSM to meet the requirements of TMT.
	Quality of the Wavefront (Cell Assembly, + Warping Harness)	Slope RMS + Subaperture stitching + Warping Harness + PSSn	Analysis + Testing	The final surface shape is increased by 71.79%@W1 62.89%@W2, 62.5%@W3, 62.80%@W4, 64.08%@W5, and 63.53% @W6 in PSSn	1) The method is feasible and effective. 2) Warping Harness is effective for improving the surface accuracy of the GSSM.

5. Conclusion

In conclusion, a novel mathematical model is established, and the mathematical relationship between the influence function of warping harness and PSSn is derived. It makes full use of the good synthesis and decomposition characteristics of PSSn and utilizes the good computational properties of Slope RMS to establish a bridge between the two indicators, providing system engineers with a good tool of error analysis and distribution. In addition, we also proposed an iterative method combining top-down evaluation method and bottom-up evaluation method which can fully evaluate the imaging quality of the system.

The validity and simplicity of the error analysis and allocation model are proved. The numerical simulations and experiments validate the effectiveness of our proposed error analysis and allocation method. The development of full-size GSSM faces world-recognized technological challenges. The experimental data of GSSMP can demonstrate the feasibility of our proposed technical processes and solutions, and lay a solid technical foundation for the next step to establish a full-size GSSM, which will greatly enhance our confidence to complete it in the future.

For a precision relay optical system, calibration can greatly reduce the construction cost. The pre-construction results of GSSM also provide substantial principle and experimental support to the research and development of the actual tertiary mirror system of TMT.

Optics EXPRESS

Funding

National Key R&D Program of China (2017YFE0102900); Youth Innovation Promotion Association of the Chinese Academy of Sciences (2016198); National Natural Science Foundation of China (NSFC) (11673080, 11403022); Jilin Science and Technology Development Program (20180520171JH).

Acknowledgements

The GSSM Research Group at CIOMP gratefully acknowledges the support of scientists and engineers from the TMT International Observatory.

Disclosures

No conflict of interest exits in the submission of this manuscript, and the final version of the manuscript has been reviewed and approved for publication by all authors. All authors agree with the submission. The work has not been published or submitted for publication elsewhere, either completely or in part, or in another form or language; no materials are reproduced from another source.

Contributions

YF, ZXJ, BS, TC, and AQC were responsible for error allocation; ZHC, MB, GPF, and JHB for positioner mechanics; GP, MC, ZJ, and CHF for cell assembly; LX, GC, QEH, HHF, and HHX for mirror polishing.

References

1. T. S. Mast and J. E. Nelson, "The Status of the W. M. Keck Observatory and Ten Meter Telescope," Proc. SPIE **571**, 226–232 (1986).
2. J. Swiegers and H. Gajjar, "Completion of the Southern African Large Telescope(SALT) Primary Mirror System," Proc. SPIE **5489**, 881–891 (2004).
3. M. W. Johns, "The Giant Magellan Telescope (GMT)," Proc. SPIE **6267**, 626729 (2006).
4. X. Cui, Y. Zhao, Y. Chu, G. Li, Q. Li, L. Zhang, H. Su, Z. Yao, Y. Wang, X. Xing, X. Li, Y. Zhu, G. Wang, B. Gu, A. Luo, X. Xu, Z. Zhang, G. Liu, H. Zhang, D. Yang, S. Cao, H. Chen, J. Chen, K. Chen, Y. Chen, J.-R. Chu, L. Feng, X.-F. Gong, Y.-H. Hou, H.-Z. Hu, N.-S. Hu, Z.-W. Hu, L. Jia, F.-H. Jiang, X. Jiang, Z.-B. Jiang, G. Jin, A.-H. Li, Y. Li, Y.-P. Li, G.-Q. Liu, Z.-G. Liu, W.-Z. Lu, Y.-D. Mao, L. Men, Y.-J. Qi, Z.-X. Qi, H.-M. Shi, Z.-H. Tang, Q.-S. Tao, D.-Q. Wang, D. Wang, G.-M. Wang, H. Wang, J.-N. Wang, J. Wang, J.-L. Wang, J.-P. Wang, L. Wang, S.-Q. Wang, Y. Wang, Y.-F. Wang, L.-Z. Xu, Y. Xu, S.-H. Yang, Y. Yu, H. Yuan, X.-Y. Yuan, C. Zhai, J. Zhang, Y.-X. Zhang, Y. Zhang, M. Zhao, F. Zhou, G.-H. Zhou, J. Zhu, and S.-C. Zou, "The Large Sky Area Multi-Object Fiber Spectroscopic Telescope (LAMOST)," Res. Astron. Astrophys. **12**(9), 1197–1242 (2012).
5. J. Nelson and G. H. Sanders, "The Status of the Thirty Meter Telescope Project," Proc. SPIE **7012**, 70121A (2008).
6. B. Sedghi, M. M. Müller, and M. Dimmler, "Analyzing the impact of vibrations on E-ELT primary segmented mirror," Proc. SPIE **9911**, 991111 (2016).
7. H. Hu, H. Zhao, Z. Liu, X. Luo, and X. Zhang, "Hydrostatic support system for in-situ optical testing of a 4 m aperture SiC mirror," Opt. Precis. Eng. **25**(10), 2607–2613 (2017).
8. F. Yang, G. Liu, Q. An and X. Zhang, "Method of evaluation of a mirror surface figure based on frequency domain and its application for the Giant Steerable Science Mirror of the Thirty Meter Telescope," Chin. Opt. Lett. **13**(4), 31–36 (2015).
9. L. Han, J. Zhang, F. Yang, and Q. An, "Estimation of the GSSM calibration error," Appl. Opt. **55**(31), 8884–8892 (2016).
10. F. Yang, H. Zhao, P. Guo, Q. An, and H. Jiang, "Pre-construction of giant steerable science mirror for TMT," Proc. SPIE **9573**, 95730T (2015).
11. B. J. Seo, C. Nissly, G. Angeli, B. Ellerbroek, J. Nelson, N. Sigrist, and M. Troy, "Analysis of Normalized Point Source Sensitivity as a Performance Metric for Large Telescopes," Appl. Opt. **48**(31), 5997–6007 (2009).
12. Q. An, J. Zhang, F. Yang, and H. Zhao, "Evaluation of the performance of the GSSM under vibration based on Normalized Point Source Sensitivity," J. Harbin Inst. Tech. **24**(5), 82–87 (2017).
13. B. J. Seo, C. Nissly, G. Angeli, B. Ellerbroek, J. Nelson, N. Sigris, and M. Troy, "Analysis of Normalized Point Source Sensitivity as a performance metric for the Thirty Meter Telescope," Proc. SPIE **7017**, 70170T (2008).
14. R. B. Schinazi, Probability with Statistical Applications (Springer, 2012), Chap. 7.
15. R. R. Nadakuditi, "Applied stochastic eigen-analysis" (Massachusetts Institute of Technology, 2007).

Optics EXPRESS

16. R. Schoenberg, "On rescaled Poisson processes and the Brownian bridge," Ann. Inst. Stat. Math. **54**(2), 445–457 (2002).
17. B. J. Seo, C. Nissly, M. Troy, G. Angeli, V. Ford, L. Stepp, and E. Williams, "Approximation of normalized point source sensitivity using power spectral density and slopes of wavefront aberration," Appl. Opt. **52**(17), 3910–3922 (2013).
18. P. Zhang, H. Zhao, B. Liu, F. Gao, and J. Huang, "Simple method for the implementation of subaperture stitching interferometry," Opt. Eng. **50**, 62–65 (2011).
19. L. Zhang, C. Tian, D. Liu, T. Shi, Y. Yang, H. Wu, and Y. Shen, "Non-null annular subaperture stitching interferometry for steep aspheric measurement," Appl. Opt. **53**(25), 5755–5762 (2014).
20. K. Q. Zhao, T. G. Bjåstad, and K. Kristoffersen, "Error analysis of subaperture processing in 1-d ultrasound arrays," IEEE Trans. Ultrason. Ferroelectr. Freq. Control **62**(4), 663–672 (2015).
21. X. Wang, "Measurement of large off-axis convex asphere by systemic stitching testing method," Chinese Optics **9**(1), 130–136 (2016).
22. P. Murphy, G. Devries, J. Fleig, G. Forbes, A. Kulawiec, and D. Miladinovic, "Measurement of high-departure aspheric surfaces using subaperture stitching with variable null optics," Proc. SPIE **7426**, 74260P (2009).
23. S. Xue, S. Chen, F. Shi, and J. Lu, "Sub-aperture stitching test of a cylindrical mirror with large aperture," Proc. SPIE **9684**, 96840C (2016).
24. H. Xu and Y. Li, "Wavefront reconstruction based on discrete sampling of sub-aperture slope," Optics and Precision Engineering **24**(1), 20–29 (2016).
25. F. Yan, B. Fan, X. Hou, and F. Wu, "Absolute subaperture testing by multiangle averaging and Zernike polynomial fitting method," Opt. Eng. **52**(8), 085101 (2013).
26. R. A. Christensen, "*Plane answers to complex questions: the theory of linear models*," *Plane Answers to Complex Questions*, (2011).
27. G. Z. Angeli, S. Roberts, and K. Vogiatzis, "Systems engineering for the preliminary design of the Thirty Meter Telescope," Proc. SPIE **7017**, 701704 (2008).
28. S. Chen, Y. Dai, S. Li, X. Peng, and J. Wang, "Error reductions for stitching test of large optical flats," Opt. Laser Technol. **44**(5), 1543–1550 (2012).
29. A. Miyashita, R. Ogasawara, N. Takato, G. Kosugi, T. Takata, and F. Uraguchi, "Temperature control for the primary mirror and seeing statistics of Subaru Telescope," Proc. SPIE **4837**, 255–263 (2003).
30. M. Otsubo, K. Okada, and J. Tsujiuchi, "Measurement of large plane surface shapes by connecting small-aperture interferograms," Opt. Eng. **33**(2), 608–613 (1994).
31. S. Roberts, J. Rogers, H. Thompson, K. Vogiatzis, D. MacMartin, E. Wilde, M. Troy, B. J. Seo, and C. Nissly, "Systems engineering of the Thirty Meter Telescope for the construction phase," Proc. SPIE **9150**, 91500V (2014).
32. L. M. Stepp, "Thirty Meter Telescope project update," Proc. SPIE **8444**, 84441G (2012).
33. F. Yang, G. Liu, H. Zhao, and J. Zhang, "Stiffness allocation and analysis of TMT M3S," Optics and Precision Engineering **24**(1), 152–159 (2016).
34. V. Ford, C. Carter, C. Delrez, P. Fumi, E. Gabriel, and D. Gallieni, "Jitter Studies for the Secondary and Tertiary Mirror Systems on the Thirty Meter Telescope," Proc. SPIE **9151**, 91512H (2014).
35. H. Zhao, J. Zhang. F. Yang, Q. An, Y. Su and P. Guo, "Study of tilt axis bearing arrangement for M3S of TMT project," Proc. SPIE **9280**, 92800M (2014).
36. J. S. Pazder, K. Vogiatzis, and G. Z. Angeli, "Dome and mirror seeing estimates for the Thirty Meter Telescope," Proc. SPIE **7017**, 70170R (2008).
37. M. Troy, G. Chanan, S. Michaels, R. Bartos, G. Bothwell, A. Give'on, R. Hein, M. Radin, J. Roberts, J. M. Rodgers, L. M. Scherr, B. J. Seo, and D. Zimmerman, "A conceptual design for the Thirty Meter Telescope Alignment and Phasing System," Proc. SPIE **7012**, 70120Y (2008).
38. G. Chanan, M.Troy, and I. Crossfield, "Predicted measurement accuracy of the TMT Alignment and Phasing System," TMT Project Communication TMT.CTR.PRE.07.007.REL01 (2007).
39. B. J. Seo, C. Nissly, M. Troy, G. Angeli, R. Bernier, L. Stepp, and E. Williams, "Estimation of normalized point-source sensitivity of segment surface specifications for extremely large telescopes," Appl. Opt. **52**(18), 4111–4122 (2013).
40. M. Schöck, T. Do, B. L. Ellerbroek, L. Gilles, G. Herriot, L. Meyer, R. Suzuki, L. Wang, and S. Yelda, "Thirty Meter Telescope Astrometry Error Budget," Proc. SPIE **9148**, 91482L (2014).
41. C. Nissly, B. J. Seo, M. Troy, G. Angeli, J. Angione, I. Crossfield, B. Ellerbroek, L. Gilles, and N. Sigrist, "High-resolution optical modeling of the Thirty Meter Telescope for systematic performance trades," Proc. SPIE **7017**, 70170U (2008).
42. F. Yang, Q. An, J. Zhang, H. Zhao, P. Guo, and H. Jiang, "Seeing metrology of large aperture mirror of telescope," Optics and Precision Engineering **25**(10), 2572–2579 (2017).
43. B. J. Seo, C. Nissly, G. Angeli, D. MacMynowski, N. Sigrist, M. Troy, and E. Williams, "Investigation of primary mirror segment's residual errors for the Thirty Meter Telescope," Proc. SPIE **7427**, 74270F (2009).
44. D. C. Redding, "MACOS manual (Modeling and Analysis for Controlled Optical Systems)," NASA JPL, D9816, internal document (1999).
45. S. Rudoler, O. Hadar, M. Fisher, and N. S. Kopeika, "Image resolution limits resulting from mechanical vibrations II – Experiment," Opt. Eng. **30**(5), 577–589 (1991).

Optics EXPRESS

46. O. Hadar, I. Dror, and N. S. Kopeika, "Image resolution limits resulting from mechanical vibrations. Part IV: real-time numerical calculation of optical transfer functions and experimental verification," Opt. Eng. **33**(2), 566–578 (1994).
47. N. S. Kopeika and D. Wulich, "Image resolution limits resulting from mechanical vibrations," Proc. SPIE **0561**(6), 529–533 (1985).